Volume 1 | Number 1 | Jan 2013 | Pages 1–100

Journal of
Materials Chemistry A

Materials for energy and sustainability
www.rsc.org/materialsA

Li⁺

ROYAL SOCIETY
OF CHEMISTRY

ROYAL SOCIETY
OF CHEMISTRY

www.rsc.org/materialsA

Facile solvothermal synthesis of ultrathin LiFe$_x$Mn$_{1-x}$PO$_4$ nanoplates as advanced cathodes with long cycle life and superior rate capability

Longhuan Liao,[a] Hongtao Wang,[a] Hui Guo,[a] Peiyi Zhu,[b] Jian Xie,[*ac] Chuanhong Jin,[a] Shichao Zhang,[d] Gaoshao Cao,[c] Tiejun Zhu[a] and Xinbing Zhao[*ac]

(Longhuan Liao and Hongtao Wang contributed equally to this work)

[a]*State Key Laboratory of Silicon Materials, School of Materials Science and Engineering, Zhejiang University, Hangzhou, 310027, P. R. China. E-mail: xiejian1977@zju.edu.cn, zhaoxb@zju.edu.cn; Fax: +86-571-87951451; Tel: +86-571-87951451*
[b]*Industrial Technology Research Institute of Zhejiang University, Hangzhou, 310058, P. R. China*
[c]*Key Laboratory of Advanced Materials and Applications for Batteries of Zhejiang Province, Hangzhou, 310027, P. R. China*
[d]*School of Materials Science and Engineering, Beijing University of Aeronautics and Astronautics, Beijing, 100191, P. R. China*

† Electronic supplementary information (ESI) available: Preparation process of LiFe$_x$Mn$_{1-x}$PO$_4$, XRD patterns of LiFe$_x$Mn$_{1-x}$PO$_4$, SEM images of LFMP-0.05 and LFMP-0.10, SEM image of LFMP-0.10-A and comparisons of rate capability and cycling stability between LFMP-0.10 and LFMP-0.10-A, EIS plots of LiFe$_x$Mn$_{1-x}$PO$_4$/C, rate capability of the LFMP-0.15-A sample tested at lower carbon content, and comparisons of cycling stability of LiFe$_x$Mn$_{1-x}$PO$_4$/C. See DOI:

Abstract

Fe doping is widely used to improve the electrochemical performance of $LiMnPO_4$ by "implanting" the merits of high rate capability and long cycle life of $LiFePO_4$ into $LiMnPO_4$. Nevertheless, great challenges still remain to obtain high-performance $LiFe_xMn_{1-x}PO_4$ at a low x value. In this work, we synthesized ultrathin $LiFe_xMn_{1-x}PO_4$ ($x\leq0.15$) nanoplates by a facile, controllable method. The plate-like $LiFe_xMn_{1-x}PO_4$ with a small lateral size (40–100 nm) and thickness (10–20 nm) exhibits high electrochemical activity, excellent rate capability and superior cycling stability after carbon coating. At a rate as high as 50 C (8.5 A g^{-1}), the $LiFe_{0.15}Mn_{0.85}PO_4$/C composite can still yield a high discharge capacity of 96.2 mAh g^{-1} where the discharge process can be completed in only 40 s. $LiFe_{0.15}Mn_{0.85}PO_4$/C can sustain a long-term cycling up to 1000 cycles at 10 C with a capacity retention close to 70%. The fast and stable cycling ability of $LiFe_xMn_{1-x}PO_4$ makes it promising applications in electric vehicles and hybrid electric vehicles.

Introduction

Olivine-structure lithium transition-metal phosphates $LiMPO_4$ (M = Fe, Mn, Co, Ni) have been extensively studied as promising cathode materials for lithium ion batteries (LIBs) due to their high theoretical capacity and structural stability, as well as safety and environmental compatibility, since the pioneering work by Goodenough group in 1997.[1–3] Compared with $LiFePO_4$ (3.45 V vs Li/Li^+), $LiMnPO_4$ is more attractive because of its higher redox potential (4.1 V vs. Li/Li^+) and thus higher energy density, showing potential applications in electric vehicles (EVs) and hybrid electric vehicles (HEVs).[4] However, $LiMnPO_4$ has lower electronic conductivity ($<10^{-10}$ S cm^{-1}) and Li^+ diffusivity than $LiFePO_4$, making it difficult to obtain high electrochemical activity.[5] Additionally, $LiMnPO_4$ also suffers from Jahn-Teller lattice distortion at Mn^{3+} sites, interfacial strain between $LiMnPO_4$ and $MnPO_4$ phases, and metastable nature of the $MnPO_4$ phase, leading to low discharge capacity, high polarization, and poor cycling stability and rate capability.[6–9]

Carbon coating, Mn-site substitution and particle size minimization are the most effective ways to overcome these limitations of $LiMnPO_4$.[10–13] Fe doping is widely accepted and most used method to "activate" $LiMnPO_4$ by "implanting" the merits of high rate capability and long cycle life of $LiFePO_4$. Through Fe doping, $LiFe_xMn_{1-x}PO_4$ can combine the excellent rate performance of $LiFePO_4$ and high potential of $LiMnPO_4$.[14–16] Previous reports have confirmed the remarkable improvement in electrochemical performance of $LiFe_xMn_{1-x}PO_4$ at high Fe concentration.[17–20] The work by Chen et al. showed that $LiFe_{0.6}Mn_{0.4}PO_4/C$ could yield a high discharge capacity of 106.3 mAh g^{-1} at 20 C, and achieve a high capacity retention of 98.9% after 100 cycles at 2 C and 200 cycles at 5 C.[17] Sun et al. reported that $LiMn_{0.5}Fe_{0.5}PO_4/C$ could deliver a specific capacity of 100 mAh g^{-1} after 300 cycles at 1 C, with a capacity retention of 95%.[19] Nevertheless, as the Fe content increases, the energy density of $LiFe_xMn_{1-x}PO_4$ will generally decrease due to the low working voltage of the Fe^{2+}/Fe^{3+} redox couple. In this regard, a low level Mn-site replacement of by $LiMnPO_4$ Fe is favorable in order to meet the requirement of high energy density, provided that the cycling stability and rate capability of $LiFe_xMn_{1-x}PO_4$ are also satisfied.

Recently, some efforts have been made to enhance the electrochemical performance of $LiMnPO_4$ by doping a small amount of Fe ($LiFe_xMn_{1-x}PO_4$, $x \leq 0.2$).[21–27] The $LiFe_{0.1}Mn_{0.9}PO_4/C$ prepared by Zuo et al. could yield capacities of 119, 97 and 68 mAh g^{-1} at 1 C, 5 C and 10 C, respectively, and it could retain 75% of its initial capacity after 100 cycles at 10 C.[23] The work from the same group indicated that $LiFe_{0.1}Mn_{0.9}PO_4$ could exhibit improved rate capability and cycling stability compared to $LiMnPO_4$ with polyacene (PAS) coating, where the $LiFe_{0.1}Mn_{0.9}PO_4/PAS$ could deliver discharge capacities of 161, 141 and 107 mAh g^{-1} at 0.1 C, 1 C and 10 C, respectively.[26] However, great challenges still remain to obtain high-performance $LiFe_xMn_{1-x}PO_4$ with low Fe concentration ($x \leq 0.2$), whose rate capability and cycling stability should be comparable with $LiFePO_4$, while energy density should be comparable with $LiMnPO_4$. Besides, facile, controllable methods are still lacking to realize the size decrease of $LiFe_xMn_{1-x}PO_4$, which is generally essential to achieve a high performance for this kind of materials.

In our previous work,[28,29] we found that thin $LiMnPO_4$ (LMP) nanoplates, synthesized from the precursor with a $LiOH/H_3PO_4/MnSO_4$ ratio of 3:1.1:1, could exhibit excellent electrochemical performance. The plate-like $LiMnPO_4$ could deliver a discharge capacity of 108.2 mAh g^{-1} at 10 C and maintain a discharge capacity of 133.5 mAh g^{-1} after 100 cycles at 0.5 C. However, its electrochemical performance is far from satisfactory for practical applications. In this work, we found that the electrochemical performance of $LiMnPO_4$ can be remarkably improved by substituting a small amount Fe at Mn sites to form $LiFe_xMn_{1-x}PO_4$ (LFMP, $x \leq 0.15$). We also found that the morphology and size of $LiMnPO_4$ can be maintained after Fe doping, and that Fe can be uniformly doped into Mn sites of $LiMnPO_4$ when we prepared the precursor solutions of $LiFePO_4$ (LFP) and $LiMnPO_4$ separately before mixing them and performing the solvothermal reactions. After carbon coating, the plate-like $LiFe_xMn_{1-x}PO_4$ materials show superior rate capability and long cycle life. $LiFe_{0.15}Mn_{0.85}PO_4/C$ can deliver discharge capacities of 130.0 mAh g^{-1} at 10 C and 96.2 mAh g^{-1} at 50 C. This material also exhibits superior cycling performance with ~70% of initial capacity retained after 1000 cycles at 10 C. The outstanding electrochemical performance of

$LiFe_xMn_{1-x}PO_4$ makes them promising cathode materials for LIBs.

Experimental section

Synthesis of $LiFe_xMn_{1-x}PO_4$ (x=0.05, 0.10, 0.15)

Detailed description on the preparation of $LiFe_xMn_{1-x}PO_4$ (LFMP) is given in the Supporting Information. The $LiFe_{0.05}Mn_{0.95}PO_4$ (LFMP-0.05), $LiFe_{0.1}Mn_{0.9}PO_4$ (LFMP-0.10) and $LiFe_{0.15}Mn_{0.85}PO_4$ (LFMP-0.15) samples were first prepared through a two-pot mixing route of the precursor solutions, namely, the precursor solution of $LiFe_xMn_{1-x}PO_4$ was prepared by mixing the respective precursor solution of $LiMnPO_4$ and $LiFePO_4$ before the solvothermal reactions. For comparison, a one-pot mixing route was also used to prepare the precursor solution of $LiFe_{0.1}Mn_{0.9}PO_4$ (LFMP-0.10-A). $LiMnPO_4$ (LMP) and $LiFePO_4$ (LFP) samples were also prepared by a similar route as LFMP-0.10-A.

Synthesis of $LiFe_xMn_{1-x}PO_4/C$ composites

For carbon coating, the solvothermal products $LiFe_xMn_{1-x}PO_4$ (x=0.05, 0.10, 0.15) and sucrose (the weight ratio of $LiFe_xMn_{1-x}PO_4$/sucrose is 2:1) were mixed in deionized water with stirring and dried at 60 ºC for 24 h. The dried mixture was fired at 600 ºC for 4 h under Ar to form $LiFe_xMn_{1-x}PO_4/C$ composites with a carbon content around 9 wt%. For clarity, the names of the carbon-coated $LiFe_xMn_{1-x}PO_4$ samples are the same as those of the corresponding solvothermal products. For comparison, a $LiFe_{0.15}Mn_{0.85}PO_4/C$ composite (LFMP-0.15-A) with 6 wt% coated carbon was also prepared by changing the $LiFe_xMn_{1-x}PO_4$/sucrose into 3:1 before firing.

Materials characterization

The phases of the products were analyzed by X-ray diffraction (XRD) on a Rigaku D/Max-2550pc powder diffractometer equipped with Cu K_α radiation (λ = 1.541 Å). The morphologies of the products were characterized by field-emission scanning electron microscope (SEM) on an S-4800 microscope. Transmission electron microscopy (TEM) characterization was performed on a JEM 2100F microscope. The high-angle annular dark-field (HAADF)-scanning transmission electron

microscopy (STEM) images and the corresponding energy dispersive X-ray spectrometry (EDX) mapping were performed on a FEI Titan G2 80-200 ChemiSTEM microscope at an acceleration voltage of 200 kV. Carbon contents in the carbon-coated $LiFe_xMn_{1-x}PO_4$ samples were determined on a Flash EA 1112 tester.

Electrochemical measurements

The electrode slurry was made by mixing 70 wt% $LiFe_xMn_{1-x}PO_4$, 20 wt% acetylene black (AB), and 10 wt% polyvinylidene fluoride (PVDF) binder in an N-methyl pyrrolidone (NMP) with magnetic stirring. The working electrodes were made by spreading the slurry onto Al foil and dried at 110 °C under vacuum overnight. The loading of active materials on Al foil is 1.4~2.0 mg. CR2025-type coin cells were assembled in an Ar-filled glove box using Li foil as the counter electrode and Celgard 2300 film as the separator. The electrolyte is 1 M $LiPF_6$ dissolved in ethylene carbonate (EC)/dimethyl carbonate (DMC) (1:1 in volume). The electrochemical performance of the cells was evaluated using a constant-current–constant-voltage (CC–CV) mode in a voltage range of 2.0–4.5 V (vs. Li/Li$^+$) on a Neware battery cycler (Shenzhen, China). The cells were charged at desired C rate (1 C = 170 mA g^{-1}) to 4.5 V, held at 4.5 V for 1 h and discharged to 2.0 V at the same rate. The capacities were calculated based on the mass of $LiFe_xMn_{1-x}PO_4$. Cyclic voltammetry (CV) measurements were carried out on a Princeton Applied Research VersaSTAT3 electrochemistry workstation between 2.0 and 4.5 V (vs. Li/Li$^+$) at various scan rates. Electrochemical impedance spectroscopy (EIS) measurements were performed on the electrochemistry workstation with an ac voltage of 10 mV amplitude over the frequency range 10^{-3}–10^6 Hz. All of the electrochemical measurements were conducted at 25 °C.

Results and discussion

The phase purity of the solvothermal products $LiFe_xMn_{1-x}PO_4$ (LFMP-0.05 for x=0.05, LFMP-0.10 for x=0.10, LFMP-0.15 for x=0.15) was checked by XRD as seen in Fig. 1. All the diffraction peaks of the three samples agree well with the olivine structure of the standard $LiMnPO_4$ with space group

pnmb (JCPDS Card no. 33−0804) with no evidence of any impurity. As a result, phase pure

$LiFe_xMn_{1-x}PO_4$ materials have formed after the solvothermal reactions. In addition, the sharp

diffraction peaks indicate good crystallization of the solvothermal products. As seen in Fig. S1, the
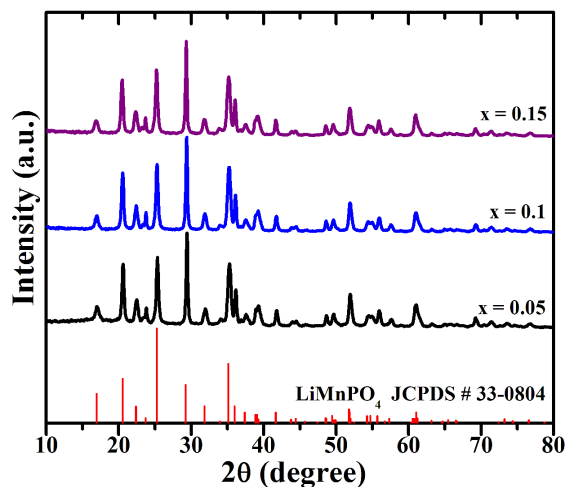
lattice parameters decrease with increased Fe/Mn ratio

Fig. 1 XRD patterns of $LiFe_xMn_{1-x}PO_4$ (*x*=0.05, 0.10, 0.15).

The morphology and microstructure are analyzed by scanning electron microscopy (SEM),

transmission electron microscopy (TEM), high-resolution TEM (HRTEM) and fast Fourier

transform (FFT). Fig. 2a gives a typical SEM image of the LFMP-0.15 sample which consists of

cuboid-like thin plates. Similar morphology can be seen in LFMP-0.05 and LFMP-0.10 (Fig. S2 in

the ESI†). TEM image in Fig. 2b indicates that the LFMP-0.15 plates have a width and length of

40–100 nm. The thickness is estimated to be 10–20 nm from some standing plates marked by the

white arrow. From some overlapped plates, we can see that the plates exhibit a transparent feature,

further revealing the ultrathin structure of the plates. Compared with the LMP,[28] no obvious size

and morphology changes in LFMP can be seen, suggesting that small amounts of Fe substitution

(≤15%) should exert minor effect on the crystal growth of LMP using this two-pot precursors

mixing method. Compared with LFMP-0.10, the LFMP-0.10-A plates exhibit a notable size

increase and a wider size distribution compared with LFMP-0.10 when using a one-pot precursors

mixing method (Fig. S3a in the ESI†). In this case, Fe doping has resulted in size rise which will

increase the diffusion length of Li ions and degrade the electrochemical performance as discussed later. This result suggests that a two-pot mixing route for precursor solutions is necessary to restrain size increase of LFMP. The HRTEM image in Fig. 2c displays that the LFMP-0.15 sample is perfectly crystallized without the formation of obvious defects after Fe doping. The interplanar spacings of 0.22 and 0.31 nm in Fig. 2c correspond to the (002) and (020) lattice planes, respectively, demonstrating that the largest exposed facet of the cuboid plates is the bc-plane, the same with LMP.[28] As seen in Fig. 2e, the thickness of carbon layer on LFMP-0.15 is rather small (below 2 nm). We can also observe discrete carbon in between the LFMP-0.15 plates (Fig. S4), which agrees with the observed relatively high carbon content in the samples. The discrete carbon also contributes to enhanced electronic conductivity of the composites by electronically connecting the LFMP particles. To obtain the insight into the crystal structure of LFMP, the LFMP-0.15 sample is further analyzed using HAADF-STEM technique. Fig. 3 presents the HAADF-STEM image of LFMP-0.15 and the corresponding EDX mapping. The mapping of Fe and Mn indicates that both Fe and Mn show a relatively uniform distribution in the sample although local aggregation of Fe occurs. This result supports that Fe has been successfully doped into Mn sites in $LiFe_{0.15}Mn_{0.85}PO_4$ crystals, which is schematically illustrated in Fig. 4.
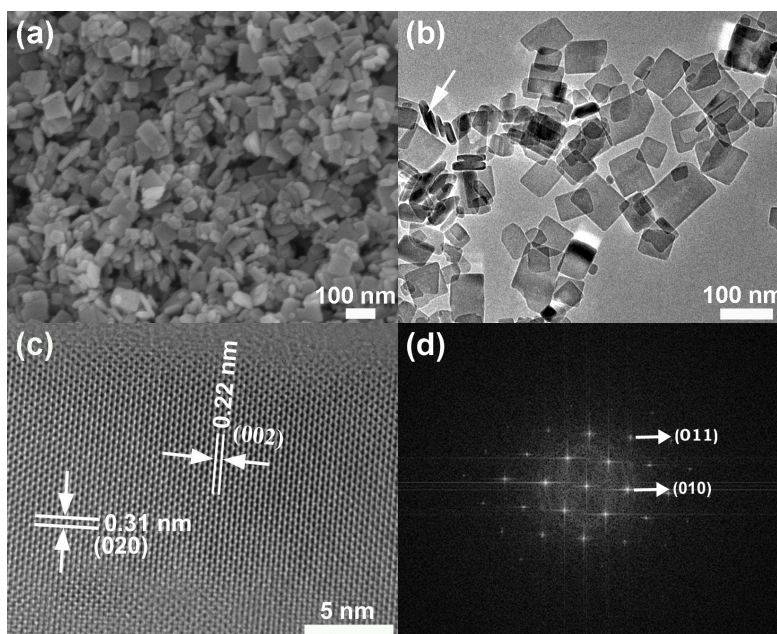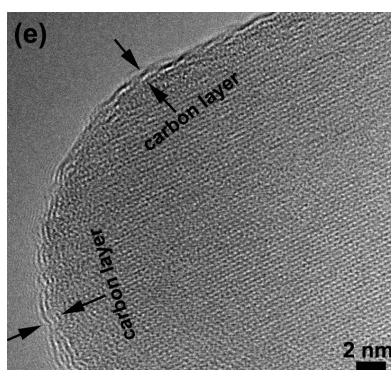
Fig. 2 (a) SEM image, (b) TEM image, (c) HRTEM image, (d) FFT patterns of the LFMP-0.15

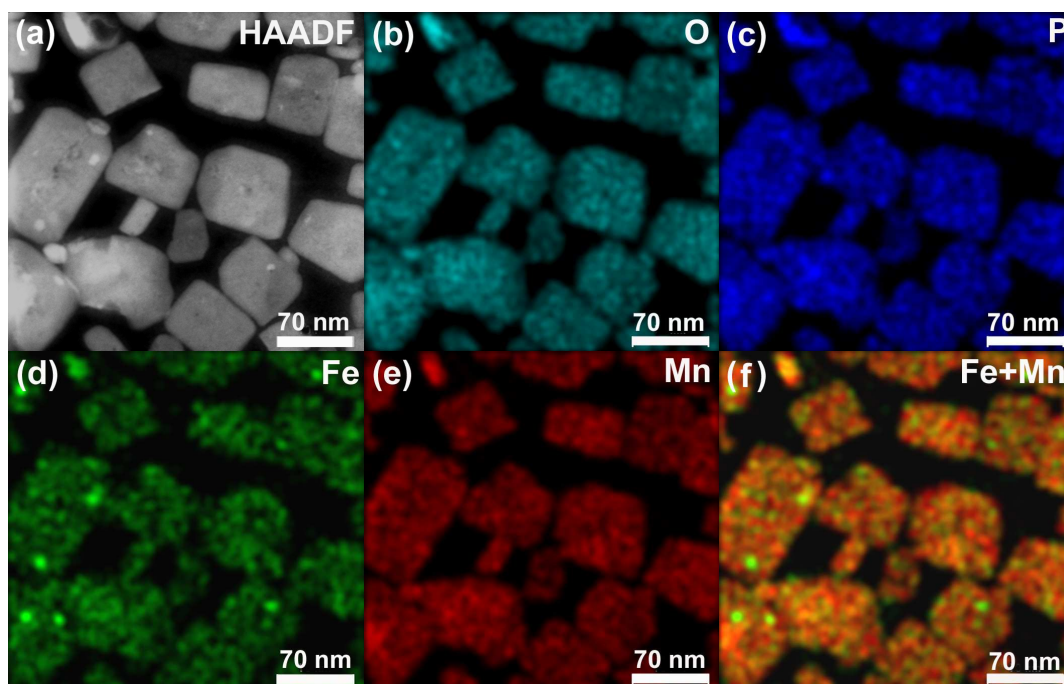sample, and (e) HRTEM image carbon-coated LFMP-0.15.

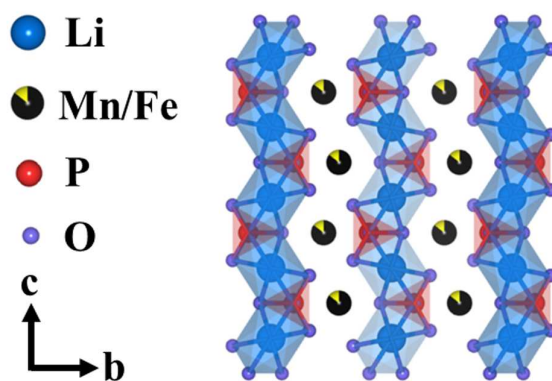**Fig. 3** (a) HAADF-STEM image and (b–f) EDX mapping of the LFMP-0.15 sample.

Fig. 4 Schematic illustration of the crystal structure of LFMP with Fe uniformly distributed in Mn

sites.

9

Fig. 5a shows the first charge-discharge curves of carbon-coated LFMP at 0.05 C. The capacities are calculated based on the weight of LFMP. All the three samples can yield high capacities at a low current density (159 mAh g^{-1} for LFMP-0.05, 164 mAh g^{-1} for LFMP-0.10, 169 mAh g^{-1} for LFMP-0.15), indicting high electrochemical activity of LFMP. Among them, LFMP-0.15 delivers the highest discharge capacity of 169 mAh g^{-1}, close to its theoretical value of 170 mAh g^{-1}. The irreversible capacities in the first cycle of LFMP-0.05, LFMP-0.10 and LFMP-0.15 are 39, 35 and 28 mAh g^{-1}. The potential plateaus at around 3.5 and 4.1 V correspond to the redox couples of Fe^{2+}/Fe^{3+} and Mn^{2+}/Mn^{3+}, respectively. As the Fe content increases, the length of 3.5 V plateau becomes longer, which proves that Fe has been successfully doped into Mn sites, agreeing with the XRD result. Fig. 5b illustrates the CV plots of the three samples at a scan rate of 0.1 mV s^{-1}. The cells were cycled for three cycles at 0.05 C prior to the CV scanning. The presence of current peak at 3.5 V further confirms the doping of Fe in Mn sites.
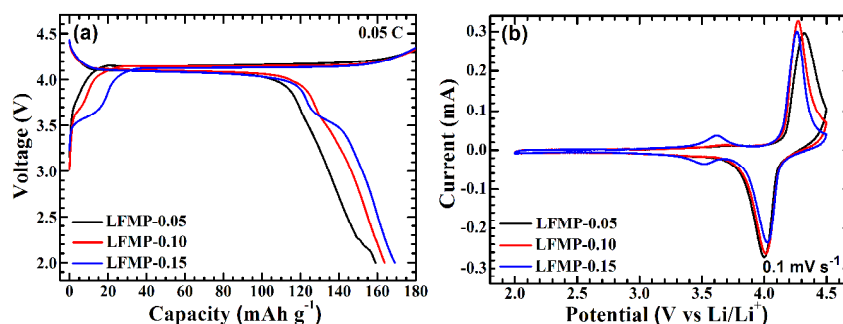

Fig. 5 (a) Voltage profiles and (b) CV scans of LiFe$_x$Mn$_{1-x}$PO$_4$/C.

Fig. 6 demonstrates the discharge profiles and rate capability of the LFMP samples at 0.1–50 C. The charge and discharge were conducted at the same current rate. As seen in the figure, the discharge capacity at each rate is on the increase with increasing the Fe content. Among the three samples, LMFP-0.15 demonstrates the best rate performance and delivers discharge capacities of 163.1, 154.8, 150.3, 146.0, 138.0, 130.0 and 120.9 mAh g^{-1} at 0.1 C, 0.5 C, 1 C, 2 C, 5 C, 10 C and 20 C, respectively. Even at 50 C, it can still yield a discharge capacity of 96.2 mAh g^{-1}, indicating excellent rate capability. At this current density, the discharge process can be completed within as

short as 40 s, while still yielding a relatively high capacity. Compared with the LMP prepared with a similar route,[28,29] the Fe-doped samples in this work exhibit better rate capability. EIS tests were performed to reveal the kinetics parameters in electrode reaction. As seen in Fig. S5a, all the impedance plots consist of a depressed semicircle at the high-to-medium frequency region and a slopping line at the low frequency region. Actually, the depressed semicircle is composed of two partially overlapped semicircles. The high-frequency semicircle is corresponds to the contact resistance (R_i) and the related capacitance (Q_1) between the current collector and active mass. The medium-frequency semicircle corresponds to charge transfer resistance (R_{ct}) and double-layer capacitance (Q_2).[30–33] The Nyquist plots are fitted using the equivalent circuit in the inset of Fig. S5a, where R_e denotes the electrolyte and ohm resistance and Z_w represents the Warburg impedance corresponding to the bulk diffusion of Li ions (low-frequency sloping line). The fitting results are summarized in Table S1. As seen in the table, the charge transfer resistance decreases as the Fe content increases. The contact resistance also decreases with increase in Fe content except LFMP-0.05. The changes of R_i and R_{ct} can also be reflected in the Bode plots (Fig. S5b,c). This suggests that Fe doping does enhance the electrode reaction kinetics, leading to improved rate capability. In addition, the small size of the LFMP is favorable for short Li-ion diffusion length, which also contributes to the excellent rate performance. This is evidenced by the better rate capability of LFMP-0.10 than LFMP-0.10-A (Fig. S3b in the ESI†). Of note is that an obvious reduction in carbon content has minor influence on the rate performance of the LFMP sample (Fig. S6 in the ESI†), meaning that the Fe-doped samples have a good intrinsic rate performance.
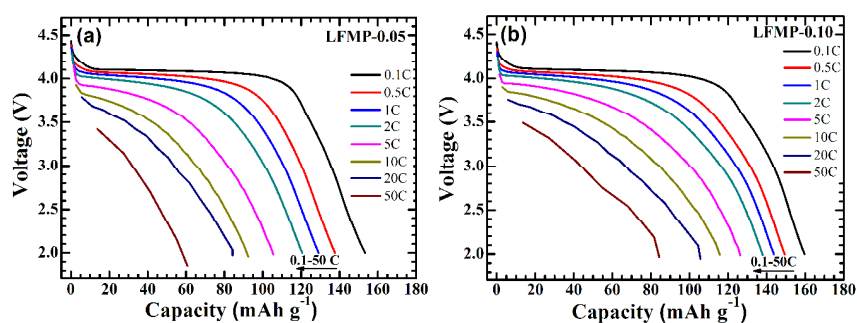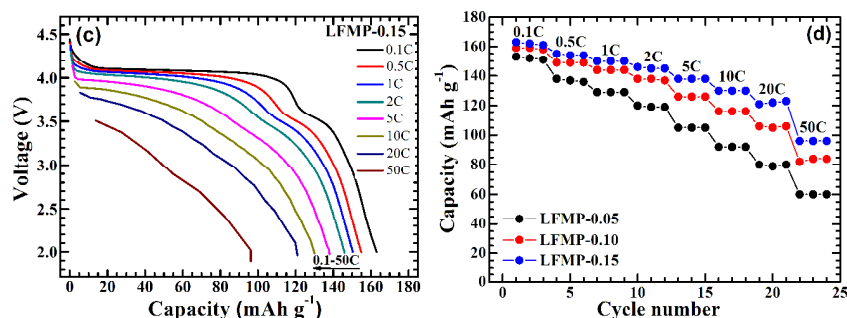
Fig. 6 Discharge profiles and rate capability of LiFe$_x$Mn$_{1-x}$PO$_4$/C.

CV measurements were conducted to further understand the different rate performance of the samples. These samples were charged and discharged at 0.05 C for three cycles prior to the CV scanning. Fig. 7 gives the CV plots of the LiFe$_x$Mn$_{1-x}$PO$_4$/C samples at various scan rates from 0.05 to 0.4 mV s^{-1}. As seen in Fig. 7d, the peak current is proportional to the square root of the scan rate, suggesting that the electrode reaction is a reversible process. For the reversible reaction, the Li-ion chemical diffusion coefficient can be calculated using the Randles Sevcik equation:[34]

$$\frac{i_p}{m} = 0.4463 n^{3/2} F^{3/2} C^* A_e R^{-1/2} T^{-1/2} D^{1/2} v^{1/2}$$

(1)

where i_p is the peak currents (A) at different scan rates, m is the mass of electrode, n is charge transfer number, F is the Faraday constant (96485 C mol^{-1}), C is the initial concentration of Li ions in LFMP (0.0223 mol cm^{-3}), A_e is the effective area (cm^2) that corresponds to the (010) planes, v is the scan rate (V s^{-1}), R is the gas constant (8.314 J mol^{-1} K^{-1}), T is the absolute temperature (298 K), and D is the chemical diffusion constant (cm^2 s^{-1}). According to the slopes of the fitting lines in Fig. 7d, the Li-ion chemical diffusion coefficients of LFMP-0.05, LFMP-0.10 and LFMP-0.15 are calculated to be 2.9×10^{-16}, 9.5×10^{-16} and 1.2×10^{-15} cm^2 s^{-1}, respectively. The LFMP-0.15 sample shows the largest Li-ion diffusion rate, endowing it with best rate performance.
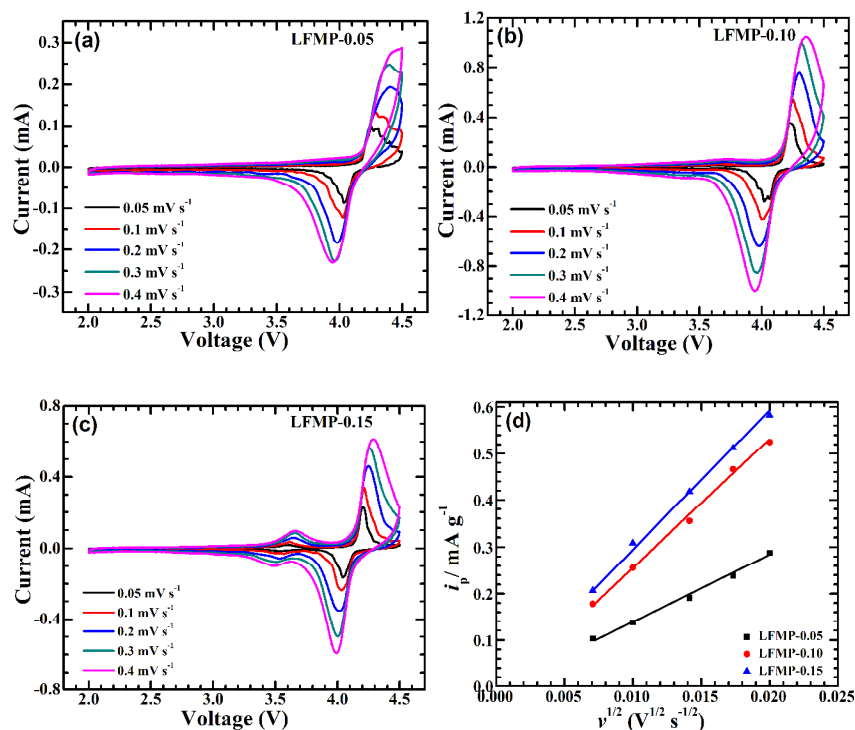
Fig. 7 CV plots of (a) LFMP-0.05, (b) LFMP-0.10 and (c) LFMP-0.15 at different scan rates, and (d) the plots of anodic peak current density (i_p) as a function of the square root of the scan rate ($v^{1/2}$).

Fig. 8a compares the rate capability of $LiFe_{0.1}Mn_{0.9}PO_4/C$ in our work and that reported previously. From the figure, we can see that the rate capability of our sample is among the best ones, due to such factors as small size, ultrathin structure, and uniform Fe doping in Mn sites. The superior rate performance of $LiFe_{0.1}Mn_{0.9}PO_4/C$ makes it promising high-power applications. Fig. 8b gives the energy density of $LiFe_xMn_{1-x}PO_4$ as a function of x at different current rates. Except LFMP-0.05, the Fe-doped samples show an increased energy density compared with the undoped one. Although the continuous increase in energy density is still possible by further increasing the Fe content, this increase trend is slowing down especially at the high-energy-density areas (0.5–2 C) with practical applications. Thus, a maximum Fe amount of $x = 0.15$ was selected to get a compromise between obtainable capacity and average working voltage, aiming at a high energy density. This suggests that the Fe doping is necessary in order to obtain a high energy density, but excess Fe doping is unnecessary and will otherwise decrease the average working voltage. At 1 C, the LFMP-0.15 sample can yield a high energy density of 581 Wh kg^{-1}, ~10% increase compared

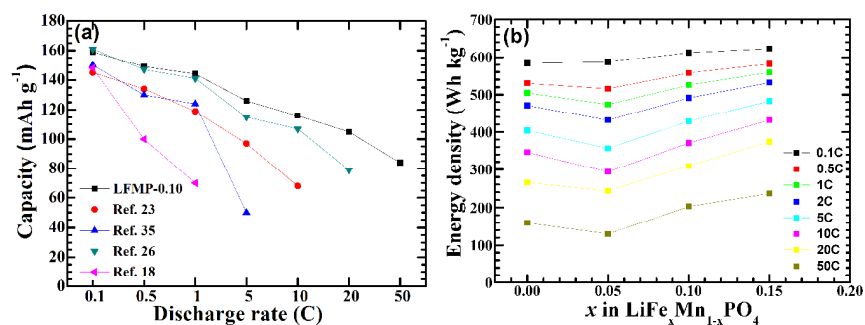with LMP, showing promising high-energy-density applications such as EVs and HEVs.

Fig. 8 Comparisons of (a) rate capability of $LiFe_{0.1}Mn_{0.9}PO_4/C$ and (b) energy density of

$LiFe_xMn_{1-x}PO_4/C$.

Fig. 9 shows the cycling stability of the LFMP samples. The cells were first charged to 4.5 V at

a given rate, held at 4.5 V for 1 h, and discharged to 2.0 V at the same rate. As seen in Fig. 8a, after

500 cycles at 1 C, LFMP-0.15, LFMP-0.10 and LFMP-0.05 can maintain high discharge capacities

of 115.7, 113.9 and 93.9 mAh g^{-1}, respectively, and the capacity retentions are all over 75%. We

notice that the LFMP-0.15 sample exhibits a higher capacity fade rate than the samples with smaller

Fe content at 1 C. It suggests that during long-term cycling, besides Mn^{2+}, Fe^{2+} also dissolves in the

electrolyte which will lead to capacity fade. Thus, it is reasonable that LFMP-0.15 exhibits rapider

capacity fade than other samples since it may lose more Fe^{2+} than others (because it has the largest

Fe content) during repeated cycling. Besides the material itself, other factors such as Li anode

corrosion and electrolyte volatilization will also affect the battery performance for a long time. At a

higher rate of 10 C, these samples can still show stable cycling (Fig. 8b). For LFMP-0.15, after

1000 cycles at 10 C, a high discharge capacity of 89.5 mAh g^{-1} is still reserved, which corresponds

to a capacity retention close to 70%, indicating its outstanding high-rate cycling stability. We also

notice that at 10 C, the three samples show a similar capacity fade rate. In this case, the Fe^{2+}

dissolution in the three samples may be similar and not significant due to low utilization of active

material and shorter cycling time at high rate. Compared with the LMP,[28,29] the LFMP samples

exhibit obviously improved cycling stability with Fe doping. As seen in Fig. 8b, during the

long-term cycling, the LFMP-0.15 sample always keeps the highest discharge capacity. It suggests

that the Fe doping not only stabilizes the crystal structure of LMP, but also improves the electrochemical activity of the Mn^{2+}/Mn^{3+} redox couple. Table S2 compares the cycling stability of some typical $LiFe_xMn_{1-x}PO_4/C$ ($x \leq 0.15$) samples in this work and others. The cycling stability of our $LiFe_xMn_{1-x}PO_4/C$ samples is among the best ones when comprehensively considering the charge/discharge rate, cycle number and carbon content. We propose that the excellent cycling stability can be attributed to uniform Fe doping in Mn sites that relieves the dissolution of Mn^{2+} and the lattice distortion. Besides, the small size and ultrathin feature of the LFMP also contribute to the high-rate cycling stability with rapid diffusion of Li ions and easy release of the lattice strain upon repeated cycling. The size effect on cycling stability is supported by Fig. S3c in Supporting Information, where LFMP-0.10-A exhibits inferior cycling stability than LFMP-0.10.
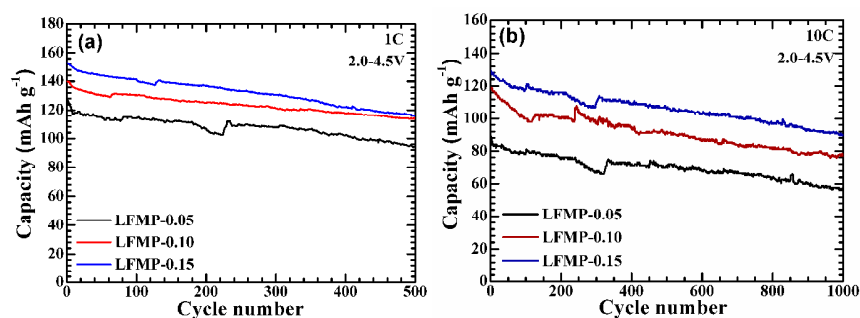

Fig. 9 Cycling stability of $LiFe_xMn_{1-x}PO_4/C$ at (a) 1 C and (b) 10 C.

Conclusions

In summary, we fabricated ultrathin $LiFe_xMn_{1-x}PO_4$ ($x \leq 0.15$) nanoplates by a facile, controllable route. Low dimension (width, length: 40–100 nm, thickness: 10–20 nm) and uniform doping of Fe in Mn sites of $LiFe_xMn_{1-x}PO_4$ can be achieved through a two-pot precursors mixing route. The $LiFe_xMn_{1-x}PO_4/C$ composites show obviously improved electrochemical activity, rate capability and cycling stability compared with $LiMnPO_4$. Among them, $LiFe_{0.15}Mn_{0.85}PO_4/C$ shows the best electrochemical performance. It exhibits excellent rate capability, delivering high discharge capacities of 138.0, 130.0 and 120.9 mAh g^{-1}, at 5 C, 10 C, and 20 C, respectively. Even at a current density as high as 50 C, it can still deliver a high discharge capacity of 96.2 mAh g^{-1}. The

excellent rate capability is ascribed to the small size and Fe-doping induced enhanced electrode kinetics. The composite also demonstrates outstanding high-rate cycling stability, maintaining ~70% of its initial capacity after 1000 cycles at 10 C. The long cycle life can be attributed to the uniform doping of Fe in Mn sites that relieves the Mn^{2+} dissolution and lattice distortion, and to the small size of the plates the facilitates the diffusion of Li ions and the release of the lattice strain. This work provides a practical and easy method to realize high electrochemical performance of $LiFe_xMn_{1-x}PO_4$ at a low Fe doping level.

Acknowledgements

References

1 C. W. Sun, S. Rajasekhara, J. B. Goodenough and F. Zhou, *J. Am. Chem. Soc.*, 2011, **133**, 2132−2135.

2 K. Saravanan, P. Balaya, M. V. Reddy, B. V. R. Chowdari and J. J. Vittal, *Energy Environ. Sci.*, 2010, **3**, 457−463.

3 A. K. Padhi, K. S. Nanjundaswamy and J. B. Goodenough, *J. Electrochem. Soc.*, 1997, **144**, 1188–1194.

4 L. Wu, J. J. Lu, G. Wei, P. F. Wang, H. Ding, J. W. Zheng, X. W. Li and S. K. Zhong, *Electrochim. Acta*, 2014, **146**, 288–294.

5 C. Delacourt, L. Laffont, R. Bouchet, C. Wurm, J. B. Leriche, M. Morcrette, J. M. Tarascon and
C. Masquelier, *J. Electrochem. Soc.*, 2005, **152**, A913–A921.

6 V. Aravindan, J. Gnanaraj, Y. S. Lee and S. Madhavi, *J. Mater. Chem. A*, 2013, **1**, 3518–3539.

7 S. P. Ong, A. Jain, G. Hautier, B. Kang and G. Ceder, *Electrochem. Commun.*, 2010, **12**,
427–430.

8 S. L. Shang, Y. Wang, Z. G. Mei, X. D. Hui and Z. K. Liu, *J. Mater. Chem.*, 2012, **22**,
1142–1149.

9 T. Drezen, N. H. Kwon, P. Bowen, I. Teerlinck, M. Isono and I. Exnar, *J. Power Sources*, 2007,
174, 949–953.

10 F. Wang, J. Yang, P. F. Gao, Y. NuLi and J. L. Wang, *J. Power Sources*, 2011, **196**,
10258–10262.

11 J. Hong, F. Wang, X. L. Wang and J. Graetz, *J. Power Sources*, 2011, **196**, 3659–3663.

12 S. M. Oh, S. W. Oh, C. S. Yoon, B. Scrosati, K. Amine and Y. K. Sun, *Adv. Funct. Mater.*, 2010,
20, 3260–3265.

13 R. von Hagen, H. Lorrmann, K. C. Möller and S. Mathur, *Adv. Energy Mater.*, 2012, **2**,
553–559.

14 H. L. Wang, Y. Yang, Y.Y. Liang, L. F. Cui, H. S. Casalongue, Y. G. Li, G. S. Hong, Y. Cui and
H. J. Dai, *Angew. Chem. Int. Ed.*, 2011, **123**, 7502–7506.

15 R. von Hagen, H. Lorrmann, K. C. Möller and S. Mathur, *Angew. Chem. Int. Ed.*, 2012, **2**,
553–559.

16 D. B. Ravnsbæk, K. Xiang, W. Xing, O. J. Borkiewicz, K. M. Wiaderek, P. Gionet, K. W.
Chapman, P. J. Chupas and Y. M. Chiang, *Nano Lett.*, 2014, **14**, 1484−1491.

17 W. Liu, P. Gao, Y. Y. Mi, J. T. Chen, H. H. Zhou and X. X. Zhang, *J. Mater. Chem. A*, 2013, **1**
2411–417.

18 L. J. Hu, B. Qiu, Y. G. Xia, Z. H. Qin, L. F. Qin, X. F. Zhou and Z. P. Liu, *J. Power Sources*,
2014, **248**, 246–252.

19 Y. J. Zhong, J. T. Li, Z. G. Wu, X. D. Guo, B.H. Zhong and S. G. Sun, *J. Power Sources*, 2013, **234**, 217–222.

20 K. Saravanan, V. Ramar, P. Balaya and J. J. Vittal, *J. Mater. Chem.*, 2011, **21**, 14925–14935.

21 Y. K. Sun, S. M. Oh, H. K. Park and B. Scrosati, *Adv. Mater.*, 2011, **23**, 5050–5054.

22 Z. J. Dai, L. Wang, X. M. He, F. P. Ye, C. C. Huang. J. J. Li, J. Gao, J. L. Wang, G. Y. Tian and M. G. Ouyang, *Electrochim. Acta*, 2013, **112**, 144–148.

23 P. J. Zuo, G. Y. Cheng, L. G. Wang, Y. L. Ma, C. Y. Du, X. Q. Cheng, Z. B. Wang and G. P. Yin, *J. Power Sources*, 2013, **243**, 872–879.

24 S. K. Martha, J. Grinblat, O. Haik, E. Zinigrad, T. Drezen, J. H. Miners, I. Exnar, A. Kay, B. Markovsky and D. Aurbach, *Angew. Chem. Int. Ed.*, 2009, **48**, 8559–8563.

25 X. Zhou, Y. F. Deng, L. N. Wan. X. S. Qin and G. H. Chen, *J. Power Sources*, 2014, **265**, 223–230.

26 L. G. Wang, P. J. Zuo, G. P. Yin, Y. L. Ma, X. Q. Cheng, C. Y. Du and Y. Z. Gao, *J. Mater. Chem. A*, 2015, **3**, 1569–1579.

27 W. C. Yang, Y. J. Bi, Y. P. Qin, Y. Liu, X. H. Zhang, B. C. Yang, Q. Wu, D. Y. Wang and S. Q. Shi, *J. Power Sources*, 2015, **275**, 785–791.

28 H. Guo, C. Y. Wu, J. Xie, S. C. Zhang, G. S. Cao and X. B. Zhao, *J. Mater. Chem. A*, 2014, **2**, 10581–10588.

29 H. Guo, C. Y. Wu, L. H. Liao, J. Xie, S. C. Zhang, P. Y. Zhu, G. S. Cao and X. B. Zhao, *Inorg. Chem.*, 2015, **54**, 667−674.

30 M. Gaberscek, J. Moskon, B. Erjavec, R. Dominko and J. Jamnik, *Electrochem. Solid-State Lett.*, 2008, **11**, A170−A174.

31 J. P. Schmidt, T. Chrobak, M. Ender, J. Illig, D. Klotz and E. Ivers Tiffée, *J. Power Sources*, 2011, **196**, 5342−5348.

32 J. Illig, M. Ender, T. Chrobak, J. P. Schmidt, D. Klotz and E. Ivers Tiffée, *J. Electrochem. Soc.*, 2012, **159**, A952−A960.

33 J. Illig, J. P. Schmidt, M. Weiss, A. Weber and E. Ivers Tiffée, *J. Power Sources*, 2013, **239**, 670
−679.

34 Y. Denis, C. Fietzek, W. Weydanz, K. Donoue, T. Inoue, H. Kurokawa and S. Fujitani, *J. Electrochem. Soc.*, 2007, **154**, A253−A257.

35 F. P. Ye, L. Wang, X. M. He, M. Fang, Z. J. Dai, J. X. Wang, C. C. Huang, F. Lian, J. L. Wang, G. Y. Tian and M. G. Ouyang, *J. Power Sources*, 2014, **253**, 143−149.

Table of contents entry

$LiFe_xMn_{1-x}PO_4$ exhibits excellent rate capability and superior cycling stability due to small size, ultrathin structure and uniform Fe doping.